Lasers in Manufacturing and Materials Processing (2022) 9:434–453
https://doi.org/10.1007/s40516-022-00179-1

Ultrafast Laser Texturing of Stainless Steel in Water and Air Environment

Leonardo Piccolo[1,2] · Zibo Wang[3] · Giovanni Lucchetta[2] · Mengyan Shen[3] · Davide Masato[1]

Accepted: 7 June 2022 / Published online: 20 July 2022

Abstract

Ultrafast laser texturing allows the generation of micro- and nanostructures on steel substrates. Laser-ablated textures show a wide range of structure geometries, from the micro to the nanoscale, which can enable plastic product functionalization. Polymer processing technologies are used to replicate mold textures on a large manufacturing scale. To enable new product functionalities, developing novel texture geometries is critical. The laser-ablated texture dimensions are primarily linked to the laser light properties, such as the laser wavelength, thus limiting the achievable structure shapes. This work uses ultrafast laser to manufacture textures in air and water environments. The effect of the different mediums on structures formation is characterized. The irradiation is performed over a wide range of fluence values. The texture geometry and characteristics are evaluated by scanning electron microscopy. For decreasing fluence values, the structures transitioned from micro bumps, to LIPSS, to nanostructures, regardless of the irradiation environment. Conversely, structure morphology is affected by the irradiation environment. The LIPSS pitch is lower for the underwater environment due to the change in the laser angle of incidence, which changes with the refraction index ratio of the air and water. A novel nano-lamellae texture was generated when irradiating the steel surface underwater at relatively low fluence. The dynamics of different LIPSS generations are discussed, considering the irradiation medium's optical, thermal, and physical properties.

Keywords Femtosecond laser · Texturing · LIPSS · Surface engineering · Nanostructures

✉ Leonardo Piccolo
leonardo.piccolo@unipd.it

[1] Department of Plastics Engineering, University of Massachusetts Lowell, Lowell, MA, USA

[2] Department of Industrial Engineering, University of Padova, Padova, Italy

[3] Department of Physics and Applied Physics, University of Massachusetts Lowell, 1 University Avenue, Lowell, MA, USA

Introduction

Micro- and nanostructures are increasingly attracting new attention for their unique capability of tailoring the surface properties of materials in different applications [1–5]. The development of functional surfaces is enabled by developing novel structures and pattern configurations. The demand for fast, reliable, economic, and green texturing techniques is constantly growing, driven by new product functionalities [6]. To activate novel capabilities on the plastic products, polymer processing replication-based technologies (e.g., injection molding, hot embossing, roll-to-roll extrusion coating) can reproduce textures that have been precedently created on mold masters [4, 7–11]. To expand the variety of new functionality, creating new texture geometries is critical with texturing technologies that must be competitive and cost-effective for tool manufacturing. Among texturing techniques, ultrafast pulsed laser texturing has emerged as a fast and reliable technology to create structures on a wide variety of materials, from soft materials to hard and brittle ones [12]. Depending on the substrate material and the irradiation parameters, ultrafast pulsed laser texturing enables the etching of various feature shapes and sizes, ranging between tens of nanometers and several micrometers [13]. Using this process, regular structures generated on the surface are referred to as Laser-Induced Periodic Surface Structures (LIPSS). The periodic structures can exhibit different shapes like lines, triangles, squares, and others [14–16]. In this work, we focus on linear LIPSS, obtained using linear laser polarization using steel as substrate material, privileging the application of the texture for polymer processing technologies.

Birnbaum first found LIPSS by irradiating semiconductors with a pulsed ruby laser [17]. The spatial periods and arrangement of the patterns are highly dependent on the properties of the laser light, such as wavelength [18] and polarization [19–21]. Therefore, multiple-wavelength laser sources are required to obtain LIPSS with different periodicities. To overcome this limitation, some researchers modified the processing conditions, such as irradiating fluence [22], beam inclination [23], number of pulses on the target surface [24], and irradiation environment [25], to change the LIPSS periods. However, LIPSS with reduced regularity have been obtained. LIPSS are classified according to the spatial period of their pattern. Depending on the laser fluence deposited over the surface, Low spatial frequency LIPSS (LSFL) or High spatial frequency LIPSS (HSFL) can be generated [26]. LSFL are structures with a period comprised between λ (laser wavelength) and $\lambda/2$. HSFL have a lower period, below $\lambda/2$ [2]. The structures obtained on metals are predominantly aligned perpendicularly to the laser beam polarization or the electrical field vector [27, 28].

Four ablation mechanisms have been proposed in the literature, namely (i) spallation, (ii) phase explosion, (iii) fragmentation, and (iv) vaporization [26]. (i) Spallation refers to material failure created by tensile stresses due to sudden changes in volume and pressure after irradiation [29]. (ii) Phase explosion happens when a metastable liquid reaches the thermodynamic point where massive nucleation occurs, breaking the liquid down into droplets and gas [30]. (iii)

Fragmentation is the process of desegregation of the superficial material due to the strain caused by the relaxation of the thermoelastic stresses [31]. (iv) Vaporization indicates the complete atomization of the surface layers when the deposited energy is higher than the cohesive energy of the target material [32]. The formation of LIPSS has been extensively studied, but a complete understanding of the phenomena occurring at the surface is still missing [33]. At first, the LIPSS formation was attributed to the interference between the incident laser light and the scattered radiation [34]. More recent research, generally accepts that the formation mechanism of LSFL is generated by the interference between the incident light and the excited surface plasmons polaritons (SPPs) [35, 36]. The theory follows important aspects regarding LSFL formation as the perpendicular direction of the structures with respect to the polarization vector, the relatively narrow range of fluences that exhibits LIPSS, and the typical slightly smaller period of the surface structures than the laser wavelength. However, the formation mechanism of the HSFL is still widely discussed in the literature, in which different theories are proposed, including Sipe's efficacy theory [37] and self-organization theory [38]. In the self-organization model, the energy input and the structure geometry are decoupled because the surface is driven to a non-equilibrium state by the energy input, and the structure's geometry is defined by the optical light properties (e.g., light polarization) [20]. In recent work [39], it is proposed that the formation of HSFL originates from the coupling of the femtosecond laser pulses and the sub-SPPs (i.e., subsurface plasmon polaritons).

As stated above, the appearance of LIPSS can be effectively controlled by varying the laser parameters. Yasumaru et al. [22] studied the LIPSS formation on titanium and chromium nitride by changing the irradiating fluence and found that the periodic structure formed upon irradiation is sensitive to the laser fluence in the near-threshold region, progressively stabilizing for higher fluences. In particular, the LIPSS period was found dependent on the laser fluence, with a positive relationship. Unlike the previous study, where linear polarization was used, Romano et al. [15] investigated the role of fluence in steel processing using circular polarization. Random, line-like, and triangular LIPSS formed over the irradiated surface scanned with different pulse fluences. The role of the number of pulses (i.e., the number of times the laser hits the same spot of the surface) has a parallel effect on the texture structures. Fluence and N pulses are often melted in one parameter, called accumulated fluence, which measures the total fluence delivered to the surface during irradiation. The accumulated fluence has a significant role in LIPSS formation, triggering diverse surface functionalities [40].

The environment around the irradiated surface was reported to influence the properties of the LIPSS pattern. The most studied substrate material is silicon, in which LIPSS were obtained in air, vacuum, and various liquids [25]. The period for structures obtained in the gas atmosphere is typically slightly lower than the laser wavelength [41]. Patterns obtained in liquids such as water, oil, ethanol, and acetone, show modified periodicities [42–44]. Ultrashort irradiation of materials immersed in liquids can also trigger undesired effects such as beam self-focusing, pulse stretching, and bubble formation [42]. By irradiating silicon in water, Shen et al. [45] found regular arrays of rods exhibiting a periodicity close to the laser wavelength (i.e., 800 nm) at moderate

fluences and a periodicity of 120 nm at low fluences. The study achieved nano spikes as small as 200 nm thick and 500 nm tall, two orders of magnitude smaller than those obtained when irradiating through air [46]. The water surrounding the surface has an optical effect on the laser path changing its incidence on the surface. Wang et al. irradiated metals and dielectrics in the water environment and found that the obtained structures were smaller than those obtained in air, but no substantial difference in the LIPSS obtained for dielectrics and metals was found [47]. Hence, they suggested that the water had a cooling effect that is more important than the heat flow in the substrate. The cooling effect of the surrounding water was recently modeled for femtosecond laser irradiation of silicon, indicating a large amount of heat removal caused by the water's latent heat of vaporization [48]. Indeed, bubbles nucleate in the water layer upon irradiation, removing heat and scattering and diffracting the laser light [44, 49].

In this work, a femtosecond laser is used to irradiate a steel surface in an air and water environment to obtain modified LIPSS periodicity starting from the same laser wavelength. A 370 fs laser source has been selected to limit the thermal phenomena on the workpiece surface upon irradiation. The surface texturing is carried out at different defocus distances to investigate the effect of the fluence delivered to the surface. The LIPSS shapes and main geometric dimensions are characterized using scanning electron microscopy (SEM). The generated surface structures are systematically studied in relation to the laser irradiating parameters and the medium properties.

Materials and Methods

Surface Generation

Sample Preparation

Laser texturing was investigated using 1.2343 steel (X37CrMoV5-1) samples, which are discs with a diameter of 25 mm and a thickness of 6 mm (Fig. 1(a)). The sample

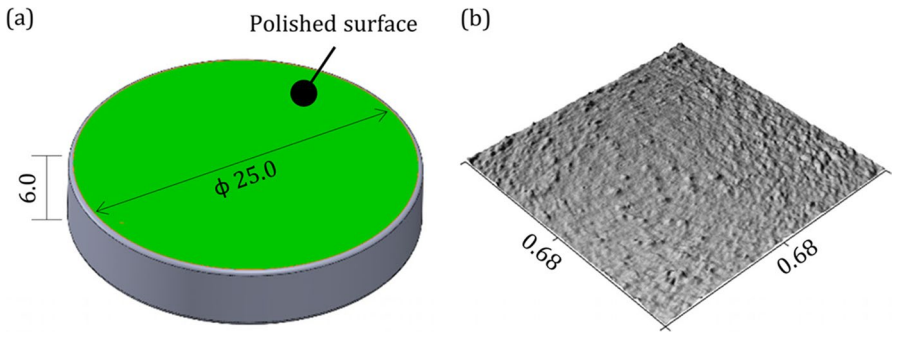

Fig. 1 (**a**) Dimensions of the steel inserts and (**b**) interferometric topography of their surface; the dimensions are in mm

surface was polished using a grinder-polisher (Buehler, Ecomet 250) to obtain a mirror-like surface finish. Interferometric optical profiling microscopy (Wiko, NT 2000) was used to measure the surface roughness of the steel samples. The surface roughness *Sa* was measured lower than 40 nm for all samples. Figure 1(b) shows a sample topography acquired for a polished sample.

Laser Equipment and Optical Setup

Laser-induced textures were generated on the sample's surface using a fixed-wavelength femtosecond laser (Spectra Physic, FemtoTrain), operating at a wavelength of 1,040 nm. The pulses emitted by the source had a duration of about 370 fs and a repetition rate of 10 MHz. The laser beam was linearly polarized and focused on the surface using a 130 mm focal length objective lens. The most significant parameters of the laser system are summarized in Table 1.

The laser scan along the sample surface was controlled using a computer-controlled two-axis translation stage equipped with stepper motors (Fig. 2). The sample was placed on the horizontal stage to allow controlled movement of the sample below the laser beam while immersed underwater. The scheme presented in Fig. 3 shows the fundamental parameters of the laser scanning path. The scan speed is intended as the speed of the laser spot along the scanning lines (that are horizontal in Fig. 3). The lateral and pulse step sizes are set to overlap the pulses along the scanning direction and between two scanning lines. The laser scanning path was designed to achieve a high overlap of the pulses (which is much higher with respect to the one presented in the figure). For all experimental conditions, the number of pulses that were superimposed over the same unit area was higher than 500. The laser polarization was directed perpendicularly to the scanning speed. For each experimental condition, 1 mm^2 of the sample surface was textured. The sample distance from the focal point was varied throughout the experiments. The Sidney Self's equations were exploited to evaluate the characteristics of the Gaussian beam [50]. The in-water dimensions of the spot were calculated considering the effect of the water refraction index on the radius of curvature of the wavefront, which shows a modified Rayleigh range on the portion of the laser beam immersed in water.

Table 1 Operating characteristics of the femtosecond laser used for the texturing experiments

Parameter	Unit	Value
Average Power	W	3.5
Central wavelength	nm	1040
Pulse duration	fs	370
Max pulse energy	μJ	0.3
Max pulse power	kW	850
Pulse repetition rate	MHz	10
Scan speed	mm/s	0.5
Beam diameter at laser source output	mm	0.6
Laser spot diameter at the focus	μm	19

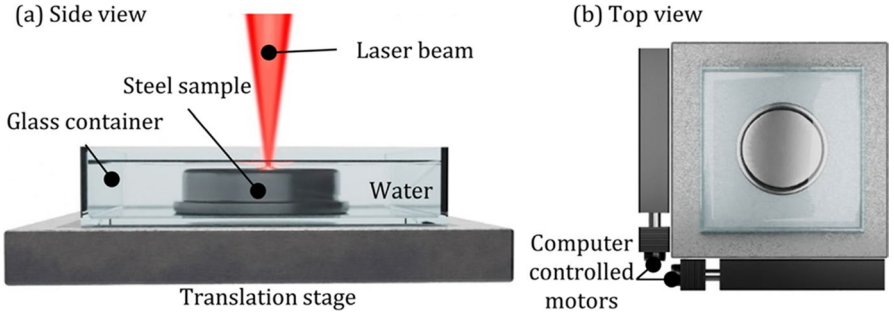

Fig. 2 Experimental setup for the laser scanning below water: the side view (**a**) underlines the small water layer over the steel sample, and the top view (**b**) shows the controlled movements present in the setup

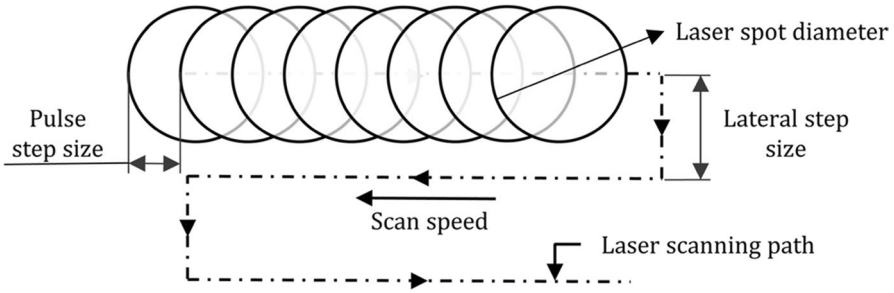

Fig. 3 Laser scanning approach and main parameters (not to scale for improved clarity)

A glass container was mounted on the stage to allow immersion of the sample in deionized water while scanning with the laser. A 1 mm layer of deionized water over the sample surface was kept constant while irradiating with laser. The water layer thickness was selected considering the results obtained by Hoppius et al. [42], which suggests that the water layer must be thicker than the air bubbles (i.e., 100 µm) formed when irradiating. Therefore, liquid surface-breaking by the generated bubbles is expected to be limited, diminishing the undesired random reflections-refractions at the uneven liquid surface. Moreover, water bubbles in the liquid bulk are undesired due to their effect on creating reflections and light tilting [49].

Texture Characterization

The morphology of the irradiated surface was evaluated by direct observation using scanning electron microscopy (SEM - Jeol, JSM 7401 F). Micrographs were acquired in four areas, evenly distributed over the irradiation area, to evaluate the texturing process's repeatability, homogeneity, and regularity. The structure periodicity was characterized by

running a 2D Fast Fourier Transform analysis of the entire measured surface. The surface periodicities were correlated to the main peaks of the spectrum [51].

The pattern quality was evaluated considering two parameters [23]: (i) regularity (R) and (ii) homogeneity. The regularity is measured as the standard deviation of the normal distribution associated with the peak of the considered periodicity. The regularity of the pattern (Eq. 1) [41] was evaluated considering the ratio between the standard deviation (σ) of the normal distribution associated with each pitch (Λ) present (Fig. 4(a)), and the pattern and the pitch itself:

$$R = 1 - \sum_{i=1}^{n} \frac{2\sigma_i}{\Lambda_i} \tag{1}$$

The homogeneity of the texture considers the dispersion angle (γ) of the pitch-related peak (Fig. 4(b)), which is linked to the deviation of the pitch orthogonally to the direction of the periodicity direction. For example, when this parameter is applied to a linearly rippled texture, it represents the deviation of the structures to the straight parallel configuration.

Water Power Loss Calculation

The presence of water on the sample's surface reduces the laser power due to absorption and reflection. Hence, the power at the water steel interface (P) is smaller than that at the air/water interface (P_0). The latter was measured using a laser power meter (Coherent, PowerMax PM30) at 3.55 W. The laser power delivered to the steel surface submerged in water can be calculated as:

$$P = P_0 \cdot (1 - R) \cdot (1 - \varepsilon) \tag{2}$$

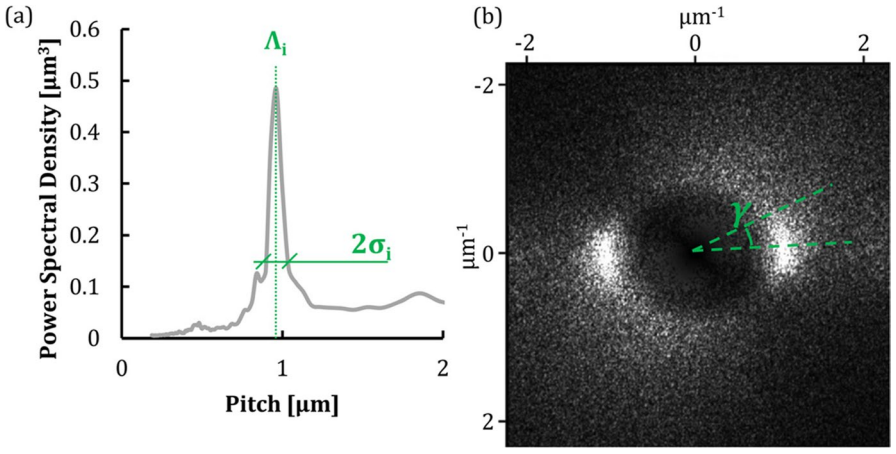

Fig. 4 (**a**) Example of a Power Spectral Density Function of a periodic texture. The standard deviation associated with the peak (at the pitch Λ_i) is highlighted. (**b**) Example of a 2DFFT of a periodic texture. The dispersion angle (γ) of the pitch-related peak is highlighted

where R is the reflectivity of the water surface, and ε is the power loss due to absorption in the water layer. The reflectivity can be calculated from the refractive index (n) and the absorption constant (k):

$$R = \frac{(n-1)^2 + k^2}{(n+1)^2 + k^2} \tag{3}$$

The power loss due to the absorption is calculated as:

$$\varepsilon_{[\%]} = \frac{P_w}{P_0} \tag{4}$$

where P_w is the power absorbed by the water thickness and is calculated from the following:

$$\frac{P_0 - P_w}{P_0} = e^{-\frac{z}{I_a}} \tag{5}$$

where I_α is the optical penetration depth of the laser beam in water:

$$I_a = \frac{\lambda}{4\pi k} \tag{6}$$

where λ is the laser wavelength, n is the refractive index, and k is the absorption constant. The resulting optical penetration depth is 30 mm. The resulting power loss for the water layer over the sample surface is then calculated as $R = 2\%$ for the reflected power and $\varepsilon = 4.5\%$ for the absorbed one.

Results and Discussion

Air Environment Irradiation

The irradiation of the steel samples in an air environment leads to different textures as a function of the laser fluence. Indeed, the laser fluence on the surface was controlled by increasing the distance of the beam from the surface with respect to a previously identified focus point. At the focal distance, the high fluence creates random microstructures (cf. Fig. 5(a)), classified as bump-like or cauliflower-like microstructures. By decreasing the laser fluence, a pattern of aligned ripples appears (cf. Fig. 5(b) obtained at a fluence of 82 mJ/cm^2). The structures are aligned perpendicularly to the laser polarization and present a slightly lower pitch than the laser wavelength. Therefore, the pattern is constituted by LSFL. The LIPSS pattern slowly faints away at lower fluence levels, and a hierarchical nano-roughness appears over less-defined LSFL (see Fig. 5(c)).

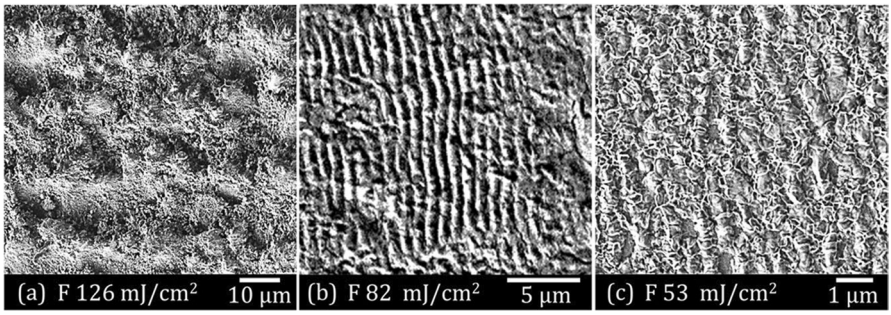

Fig. 5 SEM micrographs of the textures obtained through laser irradiation in an air environment at different fluence (F) [mJ/cm^2] values. The fluence is reported below each micrograph. Please note the different scales between the micrographs

Water Environment Irradiation

Figure 6(a) shows an SEM micrograph of a typical hierarchical layered micro-nano structure obtained when irradiating the sample in water. Random microstructures are generated on the surface, with typical dimensions ranging from 5 to 20 µm. The texture consists of repeating bumps alternating with depressions. The formation of

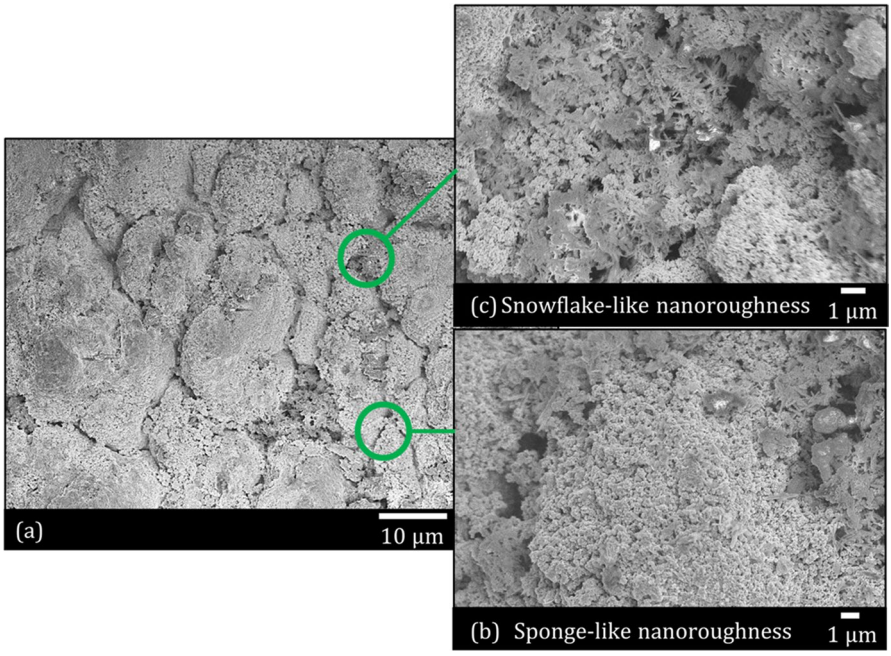

Fig. 6 (**a**) Micro-structures impressed on the steel surface with underwater laser irradiation at 117 mJ/cm^2. Magnified SEM micrographs show the different nano-texture achieved on bumps and depressions, sponge-like (**b**) and flake-like (**c**)

Fig. 7 SEM micrographs of textures obtained through irradiation in water for decreasing beam fluence ▶ from the bottom micrograph (**a**), which is at focus, diminishing the fluence from (**a**) to (**h**). The out-of-focus distance [mm] and the fluence [mJ/cm^2] are reported near the central laser beam sketch and black bottom bar. The SEM micrographs show the morphological transitions of the laser-induced structures from large bumps at high fluence to ripples, ending with finer and random textures at low fluence

these relatively big bumps can be correlated to the high fluence deposition rate on the surface.

The micro-scale texture was observed to be covered by nanoscale structures, which differ for bumps and depressions. The surface of the bumps is covered by a sponge-like nano-texture, characterized by well-distributed nano-protrusions (Fig. 6(b)). However, some micro-depressions showed a flake-like nano-texture, characterized by long and randomly oriented lamellae, presumably owing to thermal effects (Fig. 6(c)).

An ultrashort pulsed laser light passing through water may severely be altered in its properties. Beyond the consequences of the refraction index, three significant alterations of the laser process were identified. Specifically, changes were observed for (i) pulse stretching, (ii) beam self-focusing, and (iii) bubbles formation upon irradiation [42]. In this work, pulse stretching has no effect on the physical processes upon irradiation since the femtosecond pulse duration is widely below the typical electron-phonon coupling time (which is in the order of a few ps) [52]. Beam self-focusing occurs in water when the laser irradiance exceeds the threshold irradiance (i.e., 10^{12} W/cm^2) [42]. This work's maximum irradiance at focus is one magnitude lower (at $3 * 10^{11}$ W/cm^2).

Bubble formation has been reported during ultrafast laser processing of materials underwater. Micro-bubbles generate upon irradiation and persist on the surface, diffracting and scattering the light of the subsequent laser pulses. Several works report that the random distribution of the generated bubbles yields chaotic structures on the surface [25, 46, 49, 53, 54]. In this work, we focused on scanning parameters that allow for the generation of a relatively ordered linearly rippled texture, minimizing the random effect of the bubbles. Under these conditions, circularly non-ablated regions and ring-shaped microstructures indicating strong effects of the bubble on the texture were not found over the surface. However, the complex interaction between the laser light and the bubbles affects the highly random sub-micro structures (e.g., sponge-like nanostructure in Fig. 6(b)).

Effect of Laser Fluence

The size and distribution of the textures obtained underwater changed for different fluence parameters. Figure 7 shows the surface textures obtained for decreasing laser fluence. The texture geometries showed significant changes in dimensions, morphology, roughness, and regularity. The out-of-focus distance results in the enlargement of the laser spot size on the sample surface, which leads to lower fluence. The fluence obtained at the focal point was 117 mJ/cm^2. The value considers the presence of water over the sample and its effect on the laser beam reaching the surface.

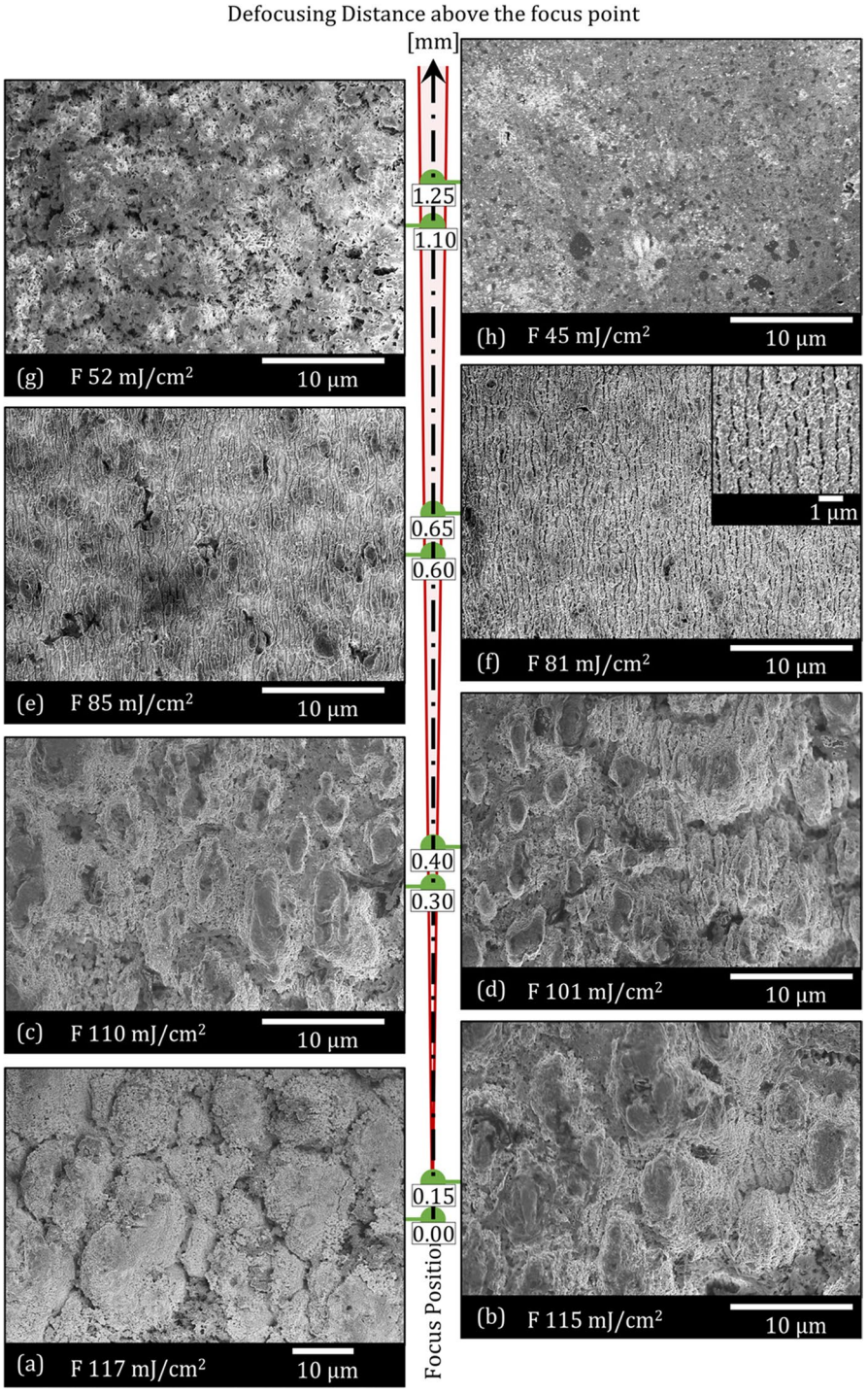
Defocusing Distance above the focus point
[mm]
1.25
1.10
0.65
0.60
0.40
0.30
0.15
0.00
Focus Position
(g) F 52 mJ/cm²
10 µm
(h) F 45 mJ/cm²
10 µm
1 µm
(e) F 85 mJ/cm²
10 µm
(f) F 81 mJ/cm²
10 µm
(c) F 110 mJ/cm²
10 µm
(d) F 101 mJ/cm²
10 µm
(a) F 117 mJ/cm²
10 µm
(b) F 115 mJ/cm²
10 µm

Close to focus, at the highest obtained fluence, the surface bumps have dimensions ranging from 10 to 30 µm. As the fluence decreases, the bumps shrink in one direction and become more like ripples (Fig. 7(d)). The surface bumps shrink in the laser polarization direction, forming structures that align perpendicularly to the polarization. The transition was continuous. The linear ripple pattern had first created between the bumps and then propagated across the surface. In particular, the texture transitioned from bumps to ripples from Fig. 7(b) (i.e. fluence of 115 mJ/cm^2) to Fig. 7(e) (i.e. fluence of 85 mJ/cm^2). For low fluence values, below 100 mJ/cm^2, the bumps are less frequent, and the homogeneity of the linear ripple pattern improved significantly (Fig. 7(f)).

When considering these morphological transitions, the obtained peak fluence at the center of the spot plays a fundamental role. At high fluence, surface bumps nucleate at specific sites and rapidly grow in size due to the superimposed pulses. This phenomenon is explained by the preferential valley ablation known in the literature as the Marangoni effect [55]. The beam-surface interaction is rather complex, but it has been divided into three fundamental components [35]:

- The hydrodynamic behavior of the molten material through the melting-solidification process.
- Thermal interaction between the lattice and the carrier.
- Electromagnetic interaction between the incident beam and the excited surface plasmon polaritons (SPPs).

The growth rate of the surface bumps is found to be a function of the peak fluence. The higher the fluence on the surface, the longer the melt lifetime and the Marangoni effect. The melt lifetime reduces by decreasing the fluence, allowing for the freezing of the excited SPPs. The duration of the SPPs depends on the wavelength of the wave itself [56]. By the time the surface re-solidifies, the SPPs characterized by lower periodicity had already died out and have been replaced by longer wavelengths. Viceversa, if the melted material cools down quickly, the SPPs freeze onto the surface, exhibiting small and homogeneous LIPSS. This is the case in Fig. 7(e) and (f), where the linear pattern created by the laser irradiation is visible. The presence of LSFL mainly characterizes the pattern. The surface crests, which are vertically aligned in Fig. 7(e) and (f), present a 90° angle with respect to the laser polarization.

Comparison of water and air environment irradiation.

The LIPSS structures generated in the air and water environment were characterized considering topographical parameters. Figure 8 reports the parameters that were evaluated from the analysis of the SEM scans. The measured pitch distance is smaller than the predicted one for both air (predicted: 1040 nm; measured: 960 nm) and water (predicted: 782 nm; measured: 680 nm) mediums. The lower periodicity (i.e., 7.7% smaller) is typical for LSFL generated in air environment [1, 57, 58]. The result obtained through water irradiation suggests a similar reduction of the periodicity (i.e., 13% smaller).

The ratio between the measured periodicities generated with different mediums is 0.71, as reported by other researchers [59]. This can be explained considering that the

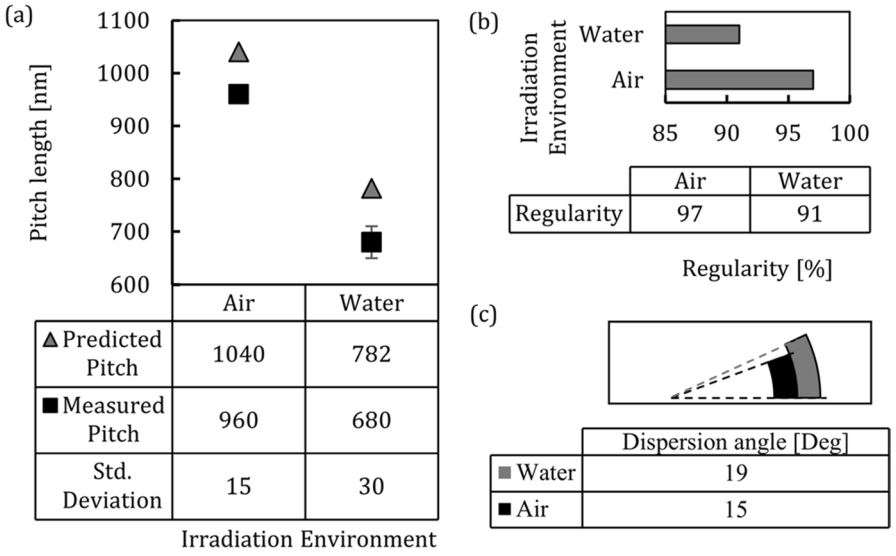

Fig. 8 Main parameters and results for interpreting the ripples pattern obtained in air and water environment. The obtained linear ripples periods are reported in (**a**). The pitch of the linear ripples is lower in water, following the variation of the refraction index. The pitch regularity (**b**) and ripples dispersion angle (**c**) show that the ripples obtained in water are less regular, which can be correlated to the presence of bubbles in the surrounding water

periodicity of the structures induced by the laser irradiation (under off-resonance [54]) correlates to the refractive index of the irradiating medium as follows [47, 54, 60]:

$$\Lambda_{pre} = \frac{\lambda}{n_{Medium}} \tag{7}$$

where Λ_{pre} is the predicted pitch distance between consecutive structures, λ is the laser wavelength, and n_{Medium} is the refractive index of the irradiation medium. Since we used the same laser source with different mediums, the refractive index ratio is equal to the predicted periodicities ratio. In fact, when using air ($n_{air}=1$) and water ($n_{water}=1.33$), the ratio between predicted periodicity ($\Lambda_{water}/\Lambda_{air}$) can be calculated at 0.75. Hence, the ratio between measured periodicities (i.e., 0.71) is close to the ratio between the refractives indexes (i.e., 0.75). The result suggests that the periodicity reduction is not dependent on the irradiation medium.

LIPSS regularity, calculated as proposed by Orazi et al. [41], is slightly higher (i.e., 6%) for the structures obtained in the air than those generated underwater (Fig. 8(b)). The homogeneity of the ripples is higher for the textures generated in the air, with a 27% reduction of the dispersion angle compared to the water environment (Fig. 8(c)). The overall lower homogeneity and regularity (see Fig. 8(b) and (c), respectively) of the textures obtained underwater can be correlated to the presence of bubbles in the water layer that can diffract and scatter light, eventually inducing non-uniform energy distribution on the treated surface [46, 49, 53].

Flake-Like Nanoscale Texture

The surface pattern became increasingly random for a fluence lower than 70 mJ/cm^2. The regular LSFL pattern disappears and is replaced by a peculiar nano-texture, similar to the flake-like structures found between the high-fluence surface bumps (cf. Fig. 6). Figure 9 shows the tiny dimensions of the flake lamellae. The length of the lamellae ranges between 1 and 3 microns, while their thickness is much smaller, around a few hundred nanometers. The infrared laser-induced texture's exceptional nano-sized surface characteristics may open up new possibilities for polymer technologies.

The nanostructures were generated on the surface at low laser fluence (cf. Fig. 7), which should not be enough to ablate the steel [26]. However, the low-power irradiation locally heats up and vaporizes tiny steel quantities on the surface, ultimately texturing the surface. The low-energy reached just a superficial layer of atoms, which got vaporized but stayed in the proximity of the surface. In between pulses, the vapor recasts onto the surface until the next pulse gets over the previously irradiated area, heating steel from the bulk again and the eventual residue of steel vapor [26]. The repetition of this process resulted in forming flake-like structures over the steel surface (cf. Fig. 9). The structures formed on the surface are randomly ordered, suggesting that their morphology does not correlate with the laser light polarization. This observation suggests that the formation mechanism involved in the formation of flake-like structures is different from the one for LSFL of HSFL.

Flake-like textures are present in nature, for example, when vapor condenses over a cold surface, forming frost. Both snow crystals and steel nanostructures appear as thin flakes spiking out of the substrate while being characterized by a different scale. The growth of the surface frost layer depends on relative humidity, the surface temperature, the presence of air, the environment temperature, and the temperature gradient that builds over the snow surface [61, 62]. When using a femtosecond laser for texturing, the steel surface is subjected to strong temperature gradients caused by the

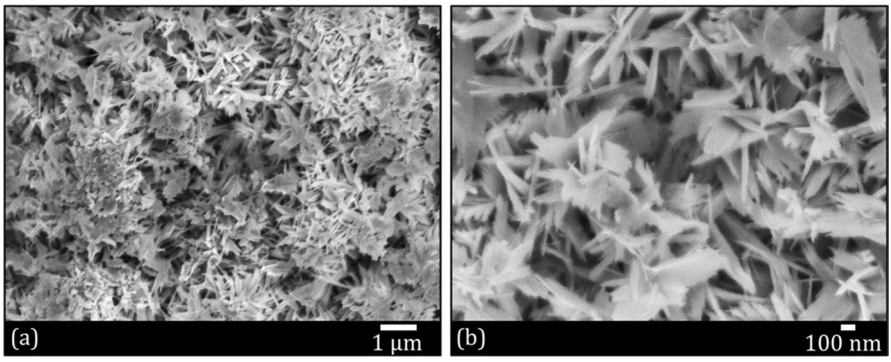

Fig. 9 Flake-like nanoscale texture generated over the micro-scale features at 52 mJ/cm^2. SEM micrographs taken at (**a**) 10,000 X and (**b**) 40,000 X

high power density of the laser pulse. The temperature gradient leads to the formation of a vaporized steel cloud over the irradiated spot (i.e., plasma plume), which is sensitive to the conditions of the surrounding environment [63].

Effect of Water on Structure Formation

Figure 10 shows the schematics of the vaporized steel cloud formation after laser irradiation in an air or water environment. A small amount of material is being vaporized at a low fluence value, leading to the formation of tiny bubbles and casts over the surface (cf. Fig. 7(h)). At high fluence, the vaporized steel cloud has higher energy, thus projecting particles away from the surface and reducing recasting. The presence of water on the irradiated surface alters the vaporized or ionized steel cloud behavior, confining the produced plasma [64]. Therefore, the plasma plumes produced during air irradiation are expected to be wider, diminishing the probability of steel recasting (cf. Fig. 10). Conversely, underwater the steel particles are kept closer to the surface, eventually promoting their quick redepositing on the substrate. The results show that this process, which we can refer to as an "ablation-recast process," is also fluence-dependent. The fluence controls the amount of ablated material and cloud energy, ultimately affecting the topography. Flake-like structures are obtained at low fluence when the recast process is decisive for forming the random structures.

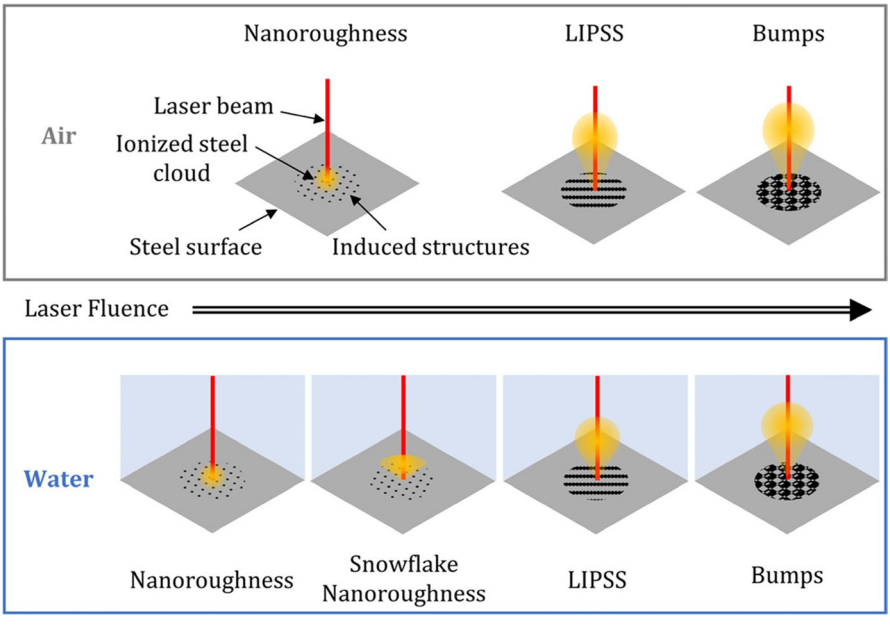

Fig. 10 Schematics of the vaporized or ionized steel cloud formation after laser irradiation

Beyond the effects of water on the ionized steel behavior, the presence of water alters the formation of surface nanostructures by oxidizing the steel surface and triggering oxides migration. Flake-like structures on different metals are obtained using the hot water treatment (HWT). However, nanometer flake-like textures were not found on steel by the authors. The authors found structures similar to those generated on Al, Bi, and bronze [65]. The formation of the structures is explained by proposing a dissolution-precipitation process in which the oxides that form over the surface migrate and redeposit onto one different surface position. In our findings, the laser light interaction with the steel/water interface and the formation of the laser-induced steel cloud deeply change the boundary conditions for the onset of the dissolution-precipitation process. Beyond the different nanostructures achieved, the surface modification obtained through laser texturing in water differs from the HWT because it occurs on a different time scale. The treatment of metal surfaces occurs in hours for HWT [65] and just a tiny fraction of a second in the case of the laser process presented here.

Overall, the combined effect of the steel cloud and the dissolution-precipitation process can be identified as the most impactful phenomena for forming flake-like structures. The laser energy deposited over the surface releases highly reactive metal atoms, rapidly reacting with water, forming oxides, and precipitating back onto the surface in self-assembled structures. The flake-like structures were observed at relatively low fluence, below the fluence for the formation of LIPSS, and in between the large bumps obtained at high fluence. The valleys between the surface bumps may limit the dispersion of the steel ions and allow for oxides redeposition, which is not found at the top of the surface bumps. At the lowest fluence, no flake-like structures are observed but a random faint nanotexture similar to the one obtained in the literature [65]. This suggests that the fluence is too low to notice differences from steel surfaces exposed to water.

Conclusions

In this work, we investigated the generation of LIPSS on steel to enable novel textures for plastic injection molding. An ultrafast laser source has been used through different irradiation mediums, namely air and deionized-water.

The results show that for air and water environments, lower fluence values yield smaller structures. At high fluence, the textures are characterized by randomly distributed micro-bumps with smaller random structures covering the micro bumps. Regular ripple patterns (LSFLs) appear for lower fluence values. Below the fluence required for the LSFLs, random nanostructures were generated. The low-fluence irradiation generated a novel flake-like texture on the steel surface only in water environment. This texture formation can be attributed to an ablation-recast process favored by the presence of water, which high density hinders the displacement of the ionized vapor cloud that forms over the irradiated surface.

Overall, the generated textures are different for the air and water environments. The ripple pattern obtained in water has a lower pitch (i.e., 680 nm) than in the air environment (i.e., 960 nm). The results are consistent with the different refraction

indexes of the two media. Moreover, the regularity was higher for ripples generated in air than water, showing a 6% difference. The dispersion angle for the patterns obtained through air is 27% lower than those generated in water, indicating higher homogeneity for the air environment.

Acknowledgements The research was supported by the Office of the Provost at the University of Massachusetts Lowell.

CRediT Authorship Contribution Statement Leonardo Piccolo: Conceptualization, Investigation, Data Curation, Writing - Original Draft, Visualization Zibo Wang: Investigation, Visualization Giovanni Lucchetta: Writing - Review & Editing Mengyan Shen: Supervision Davide Masato: Validation, Writing - Review & Editing, Supervision.

Funding Open access funding provided by Università degli Studi di Padova within the CRUI-CARE Agreement.

Data Availability All the data are available in the manuscript.

Declarations

Competing Interest The authors have no relevant financial or non-financial interests to disclose.

References

1. Bonse, J.: Quo Vadis LIPSS?—Recent and future trends on laser-induced periodic surface structures. Nanomaterials **10**, 1950 (2020). https://doi.org/10.3390/nano10101950
2. Bonse, J., Höhm, S., Kirner, S., Rosenfeld, A., Krüger, J.: Laser-induced: Periodic Surface Structures (LIPSS) – A scientific evergreen. Conf. Lasers Electro-Optics. **23**, STh1Q.3 (2016). https://doi.org/10.1364/CLEO_SI.2016.STh1Q.3
3. Orazi, L., Gnilitskyi, I., Serro, A.P.: Laser nanopatterning for wettability applications. J. Micro Nano-Manuf. **5**, 021008 (2017). https://doi.org/10.1115/1.4035956
4. Piccolo, L., Puleo, K., Sorgato, M., Lucchetta, G., Masato, D.: Modeling the replication of submicron-structured surfaces by micro injection molding. Mater. Des. **198**, 109272 (2021). https://doi.org/10.1016/j.matdes.2020.109272
5. Masato, D., Sorgato, M., Batal, A., Dimov, S., Lucchetta, G.: Thin-wall injection molding of polypropylene using molds with different laser-induced periodic surface structures. Polym. Eng. Sci. **59**, 1889–1896 (2019). https://doi.org/10.1002/pen.25189
6. Caiado, J.K.A., Piccolo, L., Sorgato, M., Lucchetta, G., Gao, P., Masato, D.: Dynamic wetting characteristics of submicron-structured injection molded parts. Polym. Eng. Sci. **62**(7), 2093–2101 (2022)

7. Masato, D., Sorgato, M., Lucchetta, G.: Characterization of the micro injection-compression molding process for the replication of high aspect ratio micro-structured surfaces. Microsyst. Technol. **23**, 3661–3670 (2017). https://doi.org/10.1007/s00542-016-3149-z
8. Sorgato, M., Masato, D., Lucchetta, G.: Effect of vacuum venting and mold wettability on the replication of micro-structured surfaces. Microsyst. Technol. **23**, 2543–2552 (2017). https://doi.org/10.1007/s00542-016-3038-5
9. Murthy, S., Matschuk, M., Huang, Q., Mandsberg, N.K., Feidenhans'L, N.A., Johansen, P., Christensen, L., Pranov, H., Kofod, G., Pedersen, H.C., Hassager, O., Taboryski, R.: Fabrication of nanostructures by roll-to-roll extrusion coating. Adv. Eng. Mater. **18**, 484–489 (2016). https://doi.org/10.1002/adem.201500347
10. Rank, A., Lang, V., Lasagni, A.F., High-Speed: Roll-to-roll hot embossing of micrometer and sub micrometer structures using seamless direct laser interference patterning treated sleeves. Adv. Eng. Mater. **19**, 1–8 (2017). https://doi.org/10.1002/adem.201700201
11. Velten, T., Bauerfeld, F., Schuck, H., Scherbaum, S., Landesberger, C., Bock, K.: Roll-to-roll hot embossing of microstructures. Microsyst. Technol. **17**, 619–627 (2011). https://doi.org/10.1007/s00542-010-1158-x
12. Sugioka, K., Cheng, Y.: Ultrafast lasers-reliable tools for advanced materials processing. Light Sci. Appl. **3**, 1–12 (2014). https://doi.org/10.1038/lsa.2014.30
13. Gräf, S.: Formation of laser-induced periodic surface structures on different materials: Fundamentals, properties and applications. Adv. Opt. Technol. **9**, 11–39 (2020). https://doi.org/10.1515/aot-2019-0062
14. Gnilitskyi, I., Derrien, T.J.Y., Levy, Y., Bulgakova, N.M., Mocek, T., Orazi, L.: High-speed manufacturing of highly regular femtosecond laser-induced periodic surface structures: Physical origin of regularity. Sci. Rep. **7**, 1–11 (2017). https://doi.org/10.1038/s41598-017-08788-z
15. Romano, J.M., Garcia-Giron, A., Penchev, P., Dimov, S.: Triangular laser-induced submicron textures for functionalising stainless steel surfaces. Appl. Surf. Sci. **440**, 162–169 (2018). https://doi.org/10.1016/j.apsusc.2018.01.086
16. Fraggelakis, F., Mincuzzi, G., Lopez, J., Manek-Hönninger, I., Kling, R.: Controlling 2D laser nano structuring over large area with double femtosecond pulses. Appl. Surf. Sci. **470**, 677–686 (2019). https://doi.org/10.1016/j.apsusc.2018.11.106
17. Birnbaum, M.: Semiconductor surface damage produced by ruby lasers. J. Appl. Phys. **36**, 3688–3689 (1965). https://doi.org/10.1063/1.1703071
18. Rodríguez-Rodríguez, Ã., Rebollar, E., Soccio, M., Ezquerra, T.A., Rueda, D.R., Garcia-Ramos, J.V., Castillejo, M., Garcia-Gutierrez, M.C.: Laser-induced periodic surface structures on conjugated polymers: Poly(3-hexylthiophene). Macromolecules **48**, 4024–4031 (2015). https://doi.org/10.1021/acs.macromol.5b00804
19. Hermens, U., Pothen, M., Winands, K., Arntz, K., Klocke, F.: Automated polarization control for the precise alignment of laser-induced self-organized nanostructures. Opt. Lasers Eng. **101**, 44–50 (2018). https://doi.org/10.1016/j.optlaseng.2017.10.001
20. Gregorčič, P., Sedlaček, M., Podgornik, B., Reif, J.: Formation of laser-induced periodic surface structures (LIPSS) on tool steel by multiple picosecond laser pulses of different polarizations. Appl. Surf. Sci. **387**, 698–706 (2016). https://doi.org/10.1016/j.apsusc.2016.06.174
21. Ouyang, J., Perrie, W., Allegre, O.J., Heil, T., Jin, Y., Fearon, E., Eckford, D., Edwardson, S.P.: Dearden G Tailored optical vector fields for ultrashort-pulse laser induced complex surface plasmon structuring. Opt. Express **23**, 12562 (2015). https://doi.org/10.1364/oe.23.012562
22. Yasumaru, N., Miyazaki, K., Kiuchi, J.: Fluence dependence of femtosecond-laser-induced nanostructure formed on TiN and CrN. Appl. Phys. A Mater. Sci. Process. **81**, 933–937 (2005). https://doi.org/10.1007/s00339-005-3218-0
23. Piccolo, L., Sorgato, M., Batal, A., Dimov, S., Lucchetta, G., Masato, D.: Functionalization of plastic parts by replication of variable pitch laser-induced periodic surface structures. Micromachines **11**, 429 (2020). https://doi.org/10.3390/mi11040429
24. Fraggelakis, F., Giannuzzi, G., Gaudiuso, C., Manek-Hönninger, I., Mincuzzi, G., Ancona, A., Kling, R.: Double- and multi-femtosecond pulses produced by birefringent crystals for the generation of 2D laser-induced structures on a stainless steel surface. Mater. (Basel). **12** (2019). https://doi.org/10.3390/ma12081257
25. Zhang, D., Sugioka, K.: Hierarchical microstructures with high spatial frequency laser induced periodic surface structures possessing different orientations created by femtosecond laser ablation of

silicon in liquids. Opto-Electron. Adv. **2**, 19000201–19000218 (2019). https://doi.org/10.29026/oea.2019.190002
26. Li, X., Guan, Y.: Theoretical fundamentals of short pulse laser – metal interaction: A review. Nanotechnol Precis Eng **3**, 105–125 (2020). https://doi.org/10.1016/j.npe.2020.08.001
27. Bonse, J., Krüger, J., Höhm, S.: Rosenfeld A Femtosecond laser-induced periodic surface structures. J. Laser Appl. **24** (2012). https://doi.org/10.2351/1.4712658
28. Moradi, S., Hatzikiriakos, S. G., Englezos, P.: Super-hydrophobic nanopatterned Interfaces: Optimization andmanufacturing (Doctoral dissertation, University of British Columbia, 2014)
29. Cheng, J., Liu, C.S., Shang, S., Liu, D., Perrie, W., Dearden, G.: Watkins K A review of ultrafast laser materials micromachining. Opt. Laser Technol. **46**, 88–102 (2013). https://doi.org/10.1016/j.optlastec.2012.06.037
30. Bulgakova, N.M., Bourakov, I.M.: Phase explosion under ultrashort pulsed laser ablation: Modeling with analysis of metastable state of melt. Appl. Surf. Sci. **197–198**, 41–44 (2002). https://doi.org/10.1016/S0169-4332(02)00300-8
31. Perez, D., Lewis, L.J.: Ablation of solids under femtosecond laser pulses. Phys. Rev. Lett. **89**, 1–4 (2002). https://doi.org/10.1103/PhysRevLett.89.255504
32. Lewis, L.J., Perez, D.: Laser ablation with short and ultrashort laser pulses: Basic mechanisms from molecular-dynamics simulations. Appl. Surf. Sci. **255**, 5101–5106 (2009). https://doi.org/10.1016/j.apsusc.2008.07.116
33. Gurevich, E.L.: Mechanisms of femtosecond LIPSS formation induced by periodic surface temperature modulation. Appl. Surf. Sci. **374**, 56–60 (2016). https://doi.org/10.1016/j.apsusc.2015.09.091
34. Stratakis, E., Bonse, J., Heitz, J., Siegel, J., Tsibidis, G.D., Skoulas, E., Papadopoulos, A., Mimidis, A., Joel, A.C., Comanns, P., Krüger, J., Florian, C., Fuentes-Edfuf, Y., Solis, J., Baumgartner, W.: Laser engineering of biomimetic surfaces. Mater. Sci. Eng. R Rep. **141**, 100562 (2020). https://doi.org/10.1016/j.mser.2020.100562
35. Tsibidis, G.D., Fotakis, C., Stratakis, E.: From ripples to spikes: A hydrodynamical mechanism to interpret femtosecond laser-induced self-assembled structures. Phys. Rev. B - Condens. Matter Mater. Phys. **92**, 1–6 (2015). https://doi.org/10.1103/PhysRevB.92.041405
36. Skolski, J.Z.P., 't Römer, G.R.B.E., Veld, A.J., Mitko, V.S., Obona, J.V., Ocelik, V., de Hosson, J.T.M.: Modeling of laser induced periodic surface structures. J. Laser Micro Nanoeng. **5**, 263–268 (2010). https://doi.org/10.2961/jlmn.2010.03.0015
37. Höhm, S., Rosenfeld, A., Krüger, J., Bonse, J.: Femtosecond laser-induced periodic surface structures on silica. J. Appl. Phys. **112** (2012). https://doi.org/10.1063/1.4730902
38. Varlamova, O., Costache, F., Reif, J., Bestehorn, M.: Self-organized pattern formation upon femtosecond laser ablation by circularly polarized light. Appl. Surf. Sci. **252**, 4702–4706 (2006). https://doi.org/10.1016/j.apsusc.2005.08.120
39. Li, Z., Wu, Q., Jiang, X., Zhou, X., Liu, Y., Hu, X., Zhang, J., Yao, J., Xu, J.: Formation mechanism of high spatial frequency laser-induced periodic surface structures and experimental support. Appl. Surf. Sci. **580**, 152107 (2022). https://doi.org/10.1016/j.apsusc.2021.152107
40. Khan, S.A., Boltaev, G.S., Iqbal, M., Kim, V., Ganeev, R.A., Alnaser, S.: Ultrafast fiber laser-induced fabrication of superhydrophobic and self-cleaning metal surfaces. Appl. Surf. Sci. **542** (2021). https://doi.org/10.1016/j.apsusc.2020.148560
41. Orazi, L., Sorgato, M., Piccolo, L., Masato, D., Lucchetta, G.: Generation and characterization of laser induced periodic surface structures on plastic injection molds. Lasers Manuf. Mater. Process. **7**, 207–221 (2020). https://doi.org/10.1007/s40516-020-00115-1
42. Hoppius, J.S., Maragkaki, S., Kanitz, A., Gregorčič, P., Gurevich, E.L.: Optimization of femtosecond laser processing in liquids. Appl. Surf. Sci. **467–468**, 255–260 (2019). https://doi.org/10.1016/j.apsusc.2018.10.121
43. Kanitz, A., Hoppius, J.S., del Mar Sanz, M., Maicas, M., Ostendorf, A., Gurevich, E.L.: Synthesis of magnetic nanoparticles by ultrashort pulsed laser ablation of iron in different liquids. Chemphyschem **18**, 1155–1164 (2017). https://doi.org/10.1002/cphc.201601252
44. Romashevskiy, S.A., Ashitkov, S.I.: Circular ripple patterns on silicon induced by bubble-diffracted femtosecond laser pulses in liquid. Opt. Lett. **45**, 1005 (2020). https://doi.org/10.1364/ol.385672
45. Shen, M., Carey, J.E., Crouch, C.H., Kandyla, M., Stone, H.A., Mazur, E., High-Density: Regular arrays of nanometer-scale rods formed on silicon surfaces via femtosecond laser irradiation in water. Nano Lett. **8**, 2087–2091 (2008). https://doi.org/10.1021/nl080291q
46. Shen, M.Y., Crouch, C.H., Carey, J.E.: Mazur E Femtosecond laser-induced formation of submicrometer spikes on silicon in water. Appl. Phys. Lett. **85**, 5694–5696 (2004). https://doi.org/10.1063/1.1828575

47. Wang, C., Huo, H., Johnson, M., Shen, M., Mazur, E.: The thresholds of surface nano-/micro-morphology modifications with femtosecond laser pulse irradiations. Nanotechnology. **21** (2010). https://doi.org/10.1088/0957-4484/21/7/075304
48. Kan, Z., Zhu, Q., Ren, H., Shen, M.: Femtosecond laser-induced thermal transport in silicon with liquid cooling bath. Mater. (Basel) **12**, 10–13 (2019). https://doi.org/10.3390/ma12132043
49. Zhang, D., Ranjan, B., Tanaka, T., Sugioka, K.: Underwater persistent bubble-assisted femtosecond laser ablation for hierarchical micro/nanostructuring. Int. J. Extrem Manuf. **2**, 015001 (2020). https://doi.org/10.1088/2631-7990/ab729f
50. Self, S.A.: Focusing of spherical Gaussian beams. Appl. Opt. **22**, 658 (1983). https://doi.org/10.1364/ao.22.000658
51. Razi, S., Ghasemi, F.: Laser-assisted generation of periodic structures on a steel surface: A method for increasing microhardness. Eur. Phys. J. Plus **133**, 1–8 (2018). https://doi.org/10.1140/epjp/i2018-11879-1
52. Gamaly, E.G., Rode, A.V., Luther-Davies, B., Tikhonchuk, V.T.: Ablation of solids by femtosecond lasers: Ablation mechanism and ablation thresholds for metals and dielectrics. Phys. Plasmas **9**, 949 (2002). https://doi.org/10.1063/1.1447555
53. Zeqin Cui, Z.C., YingqiLi, Y., Wenxian Wang, W.W., Chenghsiang Lin, C.L., Bingshe Xu, B.X.: Effect of environmental media on ablation rate of stainless steel under femtosecond laser multiple raster scans. Chin. Opt Lett **13**, 011402–011407 (2015). https://doi.org/10.3788/col201513.011402
54. Kudryashov, S.I., Nastulyavichus, A.A., Saraeva, I.N., Rudenko, A.A., Zayarny, D.A.: Ionin AA Deeply sub-wavelength laser nanopatterning of Si surface in dielectric fluids: Manipulation by surface plasmon resonance. Appl. Surf. Sci. **519**, 146204 (2020). https://doi.org/10.1016/j.apsusc.2020.146204
55. Ding, K., Wang, C., Zheng, Y., Xie, Z., Luo, Z., Man, S., Wu, B., Duan, J.: One-step fabrication of multifunctional fusiform hierarchical micro/nanostructures on copper by femtosecond laser. Surf Coat. Technol **367**, 244–251 (2019). https://doi.org/10.1016/j.surfcoat.2019.04.005
56. Shen, M.: Nanostructuring solid surfaces with femtosecond laser irradiations for applications. Mod. Phys. Lett. B **24**, 257–269 (2010). https://doi.org/10.1142/s0217984910022457
57. Li, M., Liu, M., Sun, H.: Surface nanostructuring via femtosecond lasers. Phys. Chem. Chem. Phys. **21**, 24262–24268 (2019). https://doi.org/10.1039/c9cp05351d
58. Bonse, J., Koter, R., Hartelt, M., Spaltmann, D., Pentzien, S., Höhm, S., Rosenfeld, A., Krüger, J.: Femtosecond laser-induced periodic surface structures on steel and titanium alloy for tribological applications. Appl. Phys. A Mater. Sci. Process. **117**, 103–110 (2014). https://doi.org/10.1007/s00339-014-8229-2
59. Maragkaki, S., Elkalash, A., Gurevich, E.L.: Orientation of ripples induced by ultrafast laser pulses on copper in different liquids. Appl. Phys. A Mater. Sci. Process. **123**, 1–7 (2017). https://doi.org/10.1007/s00339-017-1336-0
60. Gottmann, J., Wortmann, D., Hörstmann-Jungemann, M.: Fabrication of sub-wavelength surface ripples and in-volume nanostructures by fs-laser induced selective etching. Appl. Surf. Sci. **255**, 5641–5646 (2009). https://doi.org/10.1016/j.apsusc.2008.10.097
61. Slaughter, A.E., Adams, E.E., Staron, P.J., Shertzer, R.H., Walters, D.J., McCabe, D., Catherine, D., Henninger, I., Leonard, T., Cooperstein, M., Munter, H.: Field investigation of near-surface metamorphism of snow. J. Glaciol **57**, 441–452 (2011). https://doi.org/10.3189/002214311796905695
62. Fierz, C., Armstrong, R.L., Durand, Y., Etchevers, P., Greene, E., McClung, D.M., Nishimura, K., Satayawali, P.K., Sokratov, S.A.: The international classification for seasonal snow on the ground prepared by the ICSI-UCCS-IACS Working Group on Snow Classification. IHP-VII Tech Doc Hydrol N°83. IACS Contrib. N°1 83, 90 (2009)
63. Bogaerts, A., Chen, Z.: Effect of laser parameters on laser ablation and laser-induced plasma formation: A numerical modeling investigation. Spectrochim Acta - Part B At Spectrosc **60**, 1280–1307 (2005). https://doi.org/10.1016/j.sab.2005.06.009
64. Mak, G.Y., Lam, E.Y., Choi, H.W.: Liquid-immersion laser micromachining of GaN grown on sapphire. Appl. Phys. A Mater. Sci. Process. **102**, 441–447 (2011). https://doi.org/10.1007/s00339-010-6169-z
65. Saadi, N.S., Hassan, L.B., Karabacak, T.: Metal oxide nanostructures by a simple hot water treatment. Sci. Rep. **7**, 1–8 (2017). https://doi.org/10.1038/s41598-017-07783-8